Journal of Applied Fluid Mechanics, Vol. 15, No. 5, pp. 1403-1416, 2022.
Available online at www.jafmonline.net, ISSN 1735-3572, EISSN 1735-3645.
https://doi.org/10.47176/jafm.15.05.1211

Flow and Heat Transfer in a Co-Rotating Cavity with Tubes: A Coupled Prediction Model

W. J. Shen, S. F. Wang† and X. D. Liang

College of Energy and Power Engineering, Nanjing University of Aeronautics and Astronautics, Nanjing, Jiangsu,210016, China

†*Corresponding Author Email: sfwang@nuaa.edu.cn*

(Received March 28, 2022; accepted May 29, 2022)

ABSTRACT

In previous studies, researchers established mathematical models for predicting the pressure coefficient in simple cavities and tubed vortex reducers based on the assumptions of incompressibility and adiabatic reversibility. However, these mathematical models are not suitable for engineering design and cannot predict the internal pressure and temperature. In this study, we first derived mathematical equations for predicting the pressure drop and temperature change in a tubed vortex reducer, by considering the irreversible loss at the tube inlet. To compensate for the shortcomings of the incompressibility assumption, we developed an iterative alternating calculation method that revises the density. Subsequently, we established a coupled prediction model based on the aforementioned equations and methods. The verified Reynolds stress model results proved that the coupled prediction model and the single prediction model, which represents the incompressible case, yield similar results in predicting pressure under low-rotating-speed conditions. However, as the rotating speed was increased, the error of the single prediction model gradually increased, whereas the coupled prediction model still had good prediction accuracy. With an increase in the length and number of tubes, the pressure drop showed a decreasing trend, whereas the temperature change did not fluctuate significantly.

Keywords: Co-rotating cavity; Tube; Pressure; Temperature; Mathematical model.

NOMENCLATURE

A_t	cross-sectional area of a single tube
a	inner radius of a cavity
b	outer radius of a cavity
C_m	non-dimensional flow rate
C_p	pressure coefficient
Cp	specific heat capacity at a constant pressure
c	inlet swirl ratio
d	tube diameter
dr	radial width of the calculation cell
g	acceleration of gravity
h	specific enthalpy
m	mass flow rate
n_t	number of tubes
p	static pressure
q	specific heat
r	radial coordinate
r_{ci}	radius at the shroud orifice inlet
r_e	boundary of the source region
r_{ti}	radius at the tube inlet
r_{to}	radius at the tube outlet
Sr	swirl ratio
T	static temperature
Re_ϕ	rotational Reynolds number
V_{ri}	radial velocity
V_ϕ	circumferential velocity in a stationary frame
w	relative velocity
w_s	shaft power
x	non-dimensional radial coordinate
Z	height
θ	inclination angle of a shroud orifice
λ_T	turbulence parameter
ρ	density
μ	dynamic viscosity coefficient
ω	angular speed of a cavity

Subscripts

1	inlet of a control volume
2	outlet of a control volume
in	cavity inlet
out	cavity outlet
ϕ	circumferential direction

1. INTRODUCTION

A secondary air system (SAS) is primarily used for cooling high-temperature components, sealing between a rotor and stator, and adjusting the axial load (Chen *et al*. 2014). After the airflow is drawn centripetally from a certain stage of a high-pressure compressor, the centrifugal effect in the rotating cavity causes the airflow to produce a large pressure drop. This directly reduces the quality of the airflow and increases the flow rate of the SAS. To reduce the pressure drop, researchers have proposed tubed vortex reducers, tubeless vortex reducers, and finned vortex reducers, among which tubed vortex reducers are the most widely used.

Hide (1968) was the first to analyse the flow characteristics in a simple cavity (SC, without a vortex reducer). The flow field was divided into four regions: source region, core region, Ekman boundary layer, and sink region. Firouzian *et al*. (1985) verified the flow structure obtained by Hide (1968) by using a fluid visualisation technology. Based on the law of conservation of angular momentum and the Ekman boundary layer equation, Owen *et al*. (1985) obtained a mathematical formula for predicting the distribution of the swirl ratio, which is the ratio of the tangential velocity to the local linear velocity of the disk in the SC. Then, Firouzian *et al*. (1986) developed a mathematical model for predicting the pressure drop in an SC based on the swirl ratio formula. The results obtained by Farthing *et al*. (1989 & 1991) showed that the inlet swirl ratio, rotating Reynolds number, and non-dimensional flow rate are the key parameters that affect the pressure drop of the airflow.

In the tubed vortex reducer, the tubes are fixed in the cavity by using a support ring. Compared with the tubeless vortex reducer, the tubed vortex reducer has a more stable flow, but its weight is larger. Liang *et al*. (2015) used a combination of long and short tubes to reduce the weight. Wei *et al*. (2020) achieved the same goal by counter-rotating the air intake. Furthermore, Wei *et al*. (2019) established a mathematical model for predicting the pressure drop of a tubed vortex reducer based on the assumptions of incompressibility and adiabatic reversibility. However, the rotating speed of aeroengine shafts is high, the pressure drop can be significant, and the density and temperature can vary considerably. Therefore, treating the airflow as an incompressible fluid is unreasonable. Moreover, the velocity changes drastically at the tube inlet; thus, the irreversible loss should be considered. In this study, both the compressibility of the airflow and the irreversible loss at the tube inlet are taken into account.

Under experimental conditions, researchers usually use computational fluid dynamics (CFD) to study flow and heat transfer in a rotating cavity. Spalart and Shur (1997) proposed to modify the eddy viscosity model of one equation to increase the calculation accuracy for rotation and curvature. Torii and Yang (1995) proposed to modify the vortex viscosity model of the k-ε model to achieve the same goal. Gosman *et al.* (1976), Chew (1984), and Morse (1988) investigated the k-ε model. Their results showed that the k-ε model can predict the velocity distribution in a rotating cavity. Jones and Pascau (1989) and Poncet *et al.* (2005) reported that, in the case of a strong swirling flow, the Reynolds stress model (RSM) was better than the k-ε model because the k-ε model did not exhibit a mechanism for describing the swirling flow. Elena and Schiestel (1996) optimised the RSM under a strong swirling flow. Kumar *et al*. (2013) showed that the RSM was more suitable for high-rotating flows, whereas the k-ε and SA models were more suitable for low-rotating flows. In recent years, Onori *et al*. (2016) and Wang *et al*. (2020) have used large eddy simulations to analyse the coherent vortex structure and the vortex scale in a SC.

The pressure prediction in a cavity with radial inflow has been reported in the literature (Firouzian *et al*. 1986; Farthing *et al*. 1989 & 1991; Chew *et al*. 1989; Wei *et al*. 2019). The mathematical models have been in good agreement with experimental results. However, the validation of these models is limited by the experimental conditions. Under engineering conditions, the rotating speed of a high-pressure compressor is high. In such cases, existing models may no longer be applicable. In addition, temperature is a key parameter in the SAS. However, only a few studies have been conducted on temperature prediction, particularly for cavities with vortex reducers. In this paper, we propose an iterative alternating calculation method (IACM) to improve the pressure prediction accuracy in a tubed vortex reducer at a high rotating speed and attempt to couple the pressure and the temperature. To the best of our knowledge, this is the first study in which the irreversible loss caused by the swirling flow at the tube inlet is considered.

The subsequent sections are as follows. In Sections II and III, we introduce the physical model in detail and verify the effectiveness of grid and numerical methods. In Section IV, we describe the development of a single prediction model (SPM) and a coupled prediction model (CPM) for a tubed vortex reducer. In Section V, we explain the use of the RSM for verifying the accuracy of the SPM and CPM. Furthermore, we present an analysis of the influence of the tube structure on the pressure and temperature in the cavity. In Section VI, we provide conclusions.

2. EXPERIMENTAL SYSTEM

2.1 Air Supply System

The experiments in this study were conducted on a co-rotating cavity test bench. Figure 1 shows a schematic diagram of the test system. The compressor provides an air source for the entire test system. The air is first tranquillised in the air tank and then passed through a dryer to remove moisture. Five solenoid valves are used to control the flow rate, and vortex flow meters are used to record the values. The airflow enters a test rig from an occlusion ring and then a tubed vortex reducer through a shroud orifice.

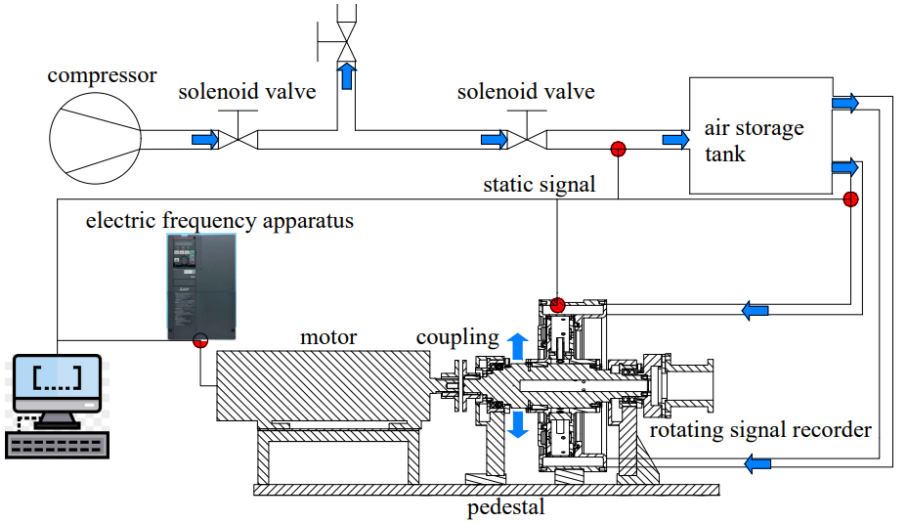

Fig. 1. Schematic diagram of the experimental system.

2.2 Test Rig and Test System

Figure 2 displays the schematic diagram of the test rig. The disk, having a thickness of 3 mm, and the shroud are fixedly connected by using bolts and then fixed on the shaft by using flat keys. The test rig is directly connected to a 15 kW three-phase AC motor through coupling. To prevent air leakage to the maximum extent, we use both a sealing labyrinth and sealing ring.

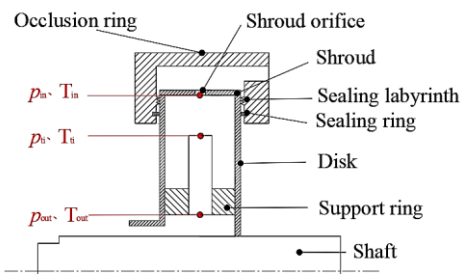

Fig. 2. Test rig.

In the tubed vortex reducer, we monitor the pressure and temperature at three radial heights: the cavity inlet, tube inlet, and tube outlet.

Owing to the limitation of the accuracy of the test instrument, a certain error is present between the measured and real data. Table 1 shows the accuracy of the test equipment. According to the definition of the non-dimensional flow rate, pressure coefficient, and error transmission theory, the maximum error of the non-dimensional flow rate is 4.2%, and the maximum error of the rotating Reynolds number is 0.322%. Under the existing test conditions, the test is conducted for only low-speed working conditions. The specific scheme is shown in Table 2.

2.3 Definition of Dimensionless Parameters

To facilitate the subsequent analysis, some non-dimensional parameters need to be defined.

The rotating Reynolds number is defined as

Table 1 Range and accuracy of the test equipment

Instrument	Range	Precision
Pressure sensor	0-0.5 MPa	±2 kPa
Flowmeter	20-1000 m^3/h	±1 m^3/h
Tachometer	2.5-99999 rpm	±1 rpm
Thermocouple	150-700 K	±0.5 K

Table 2 Experimental conditions

Parameters	Values
Rotating speed (rpm)	600, 1200, 1800, 2400, 3000
Flow rate (kg/s)	0.126

$$Re_\phi = \rho\omega b^2/\mu \tag{1}$$

Here, ρ is the density, ω is the angular velocity of the cavity, b is the outer radius of the cavity, and μ is the dynamic viscosity coefficient.

The non-dimensional flow rate is defined as

$$C_m = m/(\mu b) \tag{2}$$

Here, m is the mass flow rate.

The swirl ratio is defined as

$$Sr = V_\phi/(\omega r) \tag{3}$$

Here, V_ϕ is the tangential velocity of the airflow, and r is the radial coordinate.

3. Numeral Simulations

3.1 Simulation Model and Scheme

The simulation model is extracted based on the configuration of the test rig. To save computational resources, the fluid domain containing the tube is defined as a single simulation model, as shown in Fig. 3(a). The airflow enters the co-rotating cavity through the shroud orifice and then enters the radial passage through the tube. For the aforementioned model, we set the inlet as the pressure boundary, outlet as the flow rate boundary, wall as the adiabatic

rotating surface, and circumferential tangent surface as the periodic surface. In addition, the airflow is defined as a compressible ideal fluid.

Figure 3(b) shows a schematic diagram of the model. The outer radius of the cavity is b, inner radius is a, and axial width is S. The radius at the shroud orifice inlet is r_{ci}, and the radii at the inlet and outlet of the tubes are r_{ti} and r_{to}, respectively. All the tubes are fixed in the cavity by using a support ring. The number of the tubes is n_t. The outlet of the tubes coincides with the inner surface of the support ring. The specific dimensions are listed in Table 3.

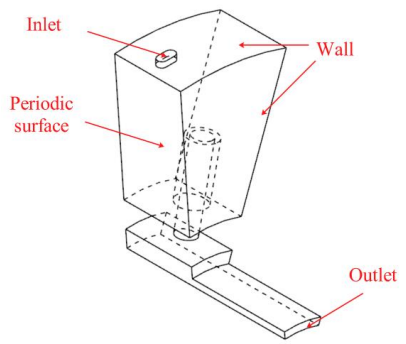

(a) Simulation model

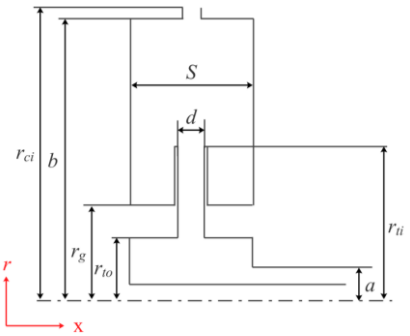

(b) Schematic diagram of the model

Fig. 3. Schematic diagram of the simulation model.

We performed a series of numerical simulations for a wide range of rotating speeds to study the importance of compressibility, as shown in Table 4. To compare the influence of high and low rotating speeds on the flow field, we selected one design point for each case. Design point 1 corresponds to 1800 rpm, and design point 2 corresponds to 16000 rpm.

Table 3 Dimensions

Parameters	Values
b	1
a/b	0.354
r_{ci}/b	1.026
r_{ti}/b	0.692, 0.744, 0.795, 0.846, 0.897, 0.949
r_{to}/b	0.385
S/b	0.256
d/b	0.069
n_t	6, 9, 12, 15, 18, 20

Table 5 presents a simulation scheme of the structural parameters. Theoretically, the length, number, and diameter of the tubes are the main parameters affecting the local loss. In particular, the change in the tube length may also have an effect on the free vortex in the cavity. Thus, we paid attention to it. In addition, according to the literature (Wei *et al.* 2019), the number and diameter of tubes have limited influence on the pressure drop in the cavity. However, the geometric analysis shows that the tube number may have a greater effect on the weight of the vortex reducer than the tube diameter. The larger the weight of the vortex reducer, the larger the overall weight which is disadvantageous for the aeroengine design. Hence, we analysed the effect of the tube number on the pressure drop and weight matching.

Table 4 Influence of the working conditions

Parameters	Values	
	Case 1	Case 2
Total pressure at the inlet (kPa)	314.865	1538
Static temperature at the inlet (K)	314.2	686
Rotating speed (rpm)	600, 1200, 1800, 2400, 3000	4000, 8000, 12000, 16000
Flow rate (kg/s)	0.126	0.3
r_{ti}/b	0.692	0.692
n_t	15	15

Table 5 Influence of the length and number of tubes

Parameters	Values	
	Tube length	Tube number
Total pressure at the inlet (kPa)	1538	1538
Static temperature at the inlet (K)	686	686
Rotating speed (rpm)	8000, 12000, 16000	8000, 12000, 16000
Flow rate (kg/s)	0.3	0.3
r_{ti}/b	0.692, 0.744, 0.795, 0.846, 0.897, 0.949	0.692
n_t	15	6, 9, 12, 15, 18, 20

3.2 Numerical method and grid

The RSM was used to study the flow characteristics in this study. The RSM abandons the concept of turbulent viscosity, directly establishes the Reynolds stress transport equation, and solves the pulsation correlation term, thereby improving the performance of the RSM for complex rotating flows. Near the wall, a scalable wall function is adopted.

Unstructured grids are used to divide the computational domain, as shown in Fig. 4. The height of the first layer near the wall is $8.2 \times 10^{-4}b$ to ensure that y^+ is in the range of 30-100. Figure 5 shows the influence of the number of grids on the results at design point 2.

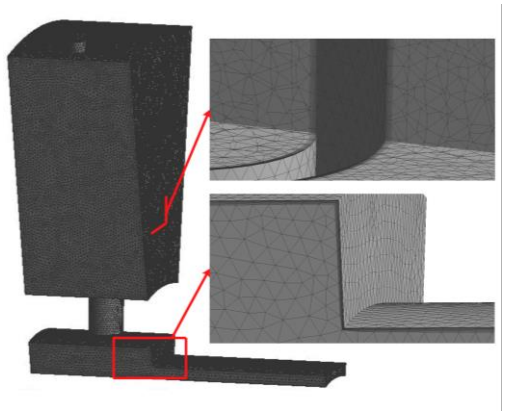

Fig. 4. Schematic of the grid.

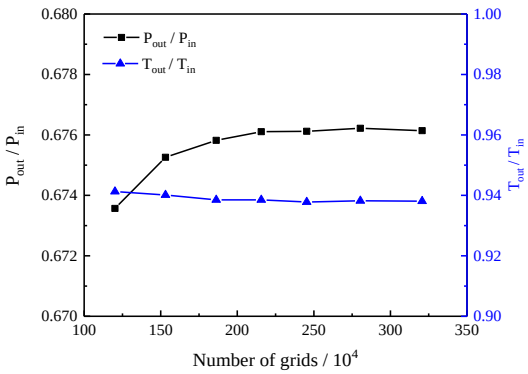

Fig. 5. Influence of the number of grids.

As the number of grids is increased, the pressure ratio first increases and then flattens, whereas the temperature ratio first decreases and then flattens. To save computing resources, the total number of grids of the model at design point 2 was set to 2.5 million, whereas the maximum size of the volume grid was $6.12\times10^{-3}b$. The same grid settings were used to study the effects of the number and length of tubes.

3.3 Model Validation

An experimental case of a SC, studied by Firouzian *et al*. (1986), was used to verify the validity of the numerical settings in the present study. Figure 6 shows a comparison of the RSM results with mathematical model results (Owen *et al*. 1985) and test results (Firouzian *et al.* 1986). For the case of Re_ϕ=4×10^5 and C_m=946, the average relative error between the CFD results and the experiments was 9.52%. To consider the difference between simple cavities and tubed vortex reducers, we experimentally verified our model in case 1. The results are shown in Figs. 7 and 8. The average relative error of the pressure ratio is 0.281%, and that of the temperature ratio is 0.047%. Overall, the RSM can sufficiently reflect changes in the pressure and temperature of the tubed vortex reducer.

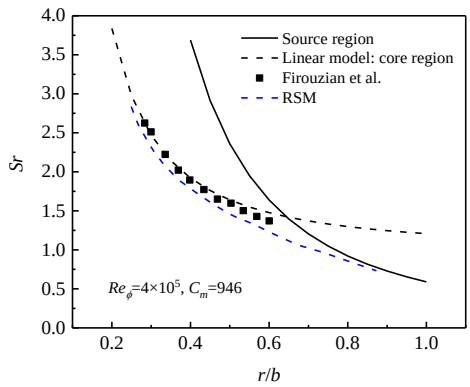

Fig. 6. Swirl ratio.

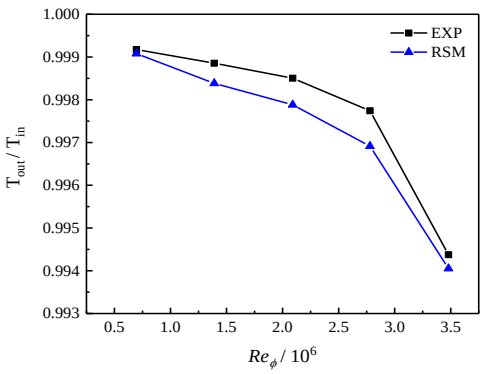

Fig.7. Pressure ratio.

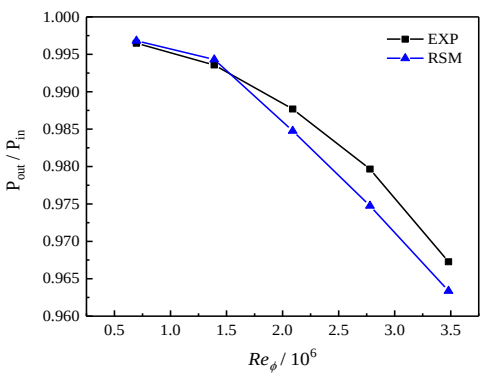

Fig. 8. Temperature ratio.

3.4 Flow Structure in the Tubed Vortex Reducer

Before a description of the theoretical analysis is provided, the flow structure in the tubed vortex

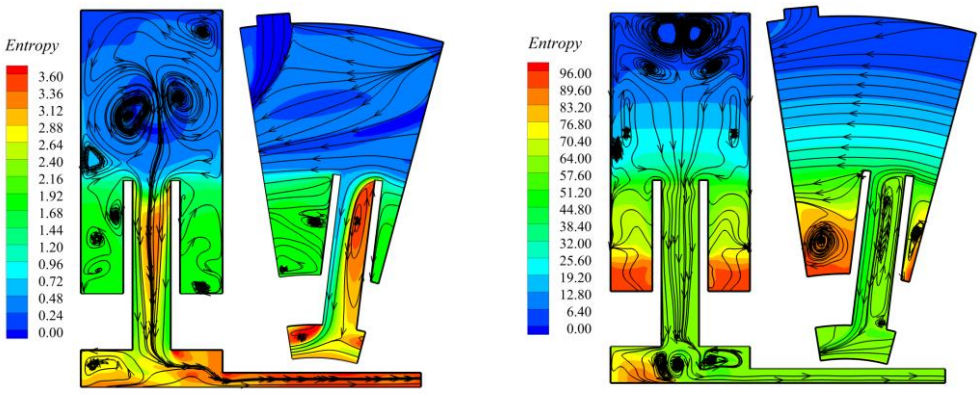

(a) Design point 1 (b) Design point 2

Fig. 9. Distribution of streamlines and entropy in the tubed vortex reducer.

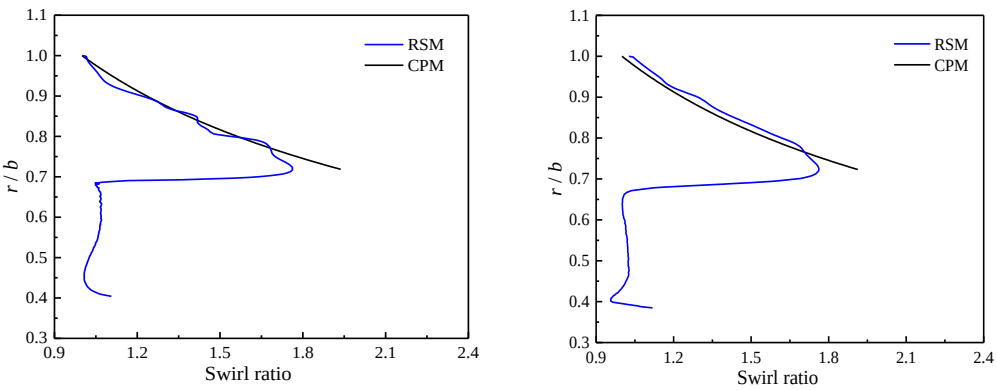

(a) Design point 1 (b) Design point 2

Fig. 10. Distribution of the swirl ratio in the radial direction of the tubed vortex reducer.

reducer should be understood. Figure 9 shows the distribution of streamlines and entropy in the tubed vortex reducer at design points 1 and 2. Owing to the effect of the Coriolis force, the airflow is gradually deflected in the direction of rotation after entering the cavity. When the airflow enters the tube, owing to the existence of the relative tangential velocity, the airflow forms a vortex at the inlet section of the tube. In addition, as the rotation speed is increased, the relative tangential velocity increases. Thus, the vortex expands downward. In the source region, the entropy does not increase significantly. Conversely, owing to the large relative velocity between the fluid layers, a significant entropy increase occurs in the Ekman boundary layer and the core region. At the tube inlet, the entropy of the airflow increases rapidly owing to the obstruction and dissipation of the vortex.

Figure 10 shows the distribution of the swirl ratio in the tubed vortex reducer at design points 1 and 2. The theoretical formulas are derived in the following section. In the cavity above the tube, the airflow is not obstructed, and the swirl ratio increases rapidly with a decrease in the radius. When the airflow reaches the tube inlet, the swirl ratio rapidly decreases over a short radial distance. In the tube, the tangential flow of the airflow is suppressed such that the swirl ratio is maintained near 1.

4. ESTABLISHMENT OF THE COUPLED PREDICTION MODEL

4.1 IACM

Under engineering conditions, the airflow in the cavity is compressible. The compressible fluid equations require many inputs and may only provide numerical solutions at the cost of the computational time. In the incompressible fluid equations, the fixed density does not agree with the real results. Hence, we propose the IACM to compensate for the flaws of the incompressibility assumption in the incompressible fluid equations. In this study, the mathematical model involving the IACM, incompressible pressure equations, and temperature equations was defined as the CPM, and the SPM involved only incompressible pressure equations. Compared with the CPM, the SPM does not consider the compressibility of the fluid and cannot predict the temperature of the airflow.

Before developing the IACM, we divided the computing domain, as shown in Fig. 11. The tubed vortex reducer was divided evenly along the radial direction, and the radial width of a single ring (calculation cell) was *dr*. In the calculation cell, the airflow was regarded as an incompressible fluid. Theoretically, when *dr* is infinitely small, the airflow

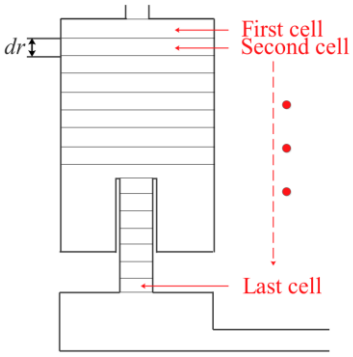

Fig. 11. Schematic diagram of the division of calculation cells in the tubed vortex reducer.

within a single cell can be considered as an incompressible fluid overall.

After the cells are divided, the cell-to-cell alternation calculation begins. Figure 12 shows a flow chart of the IACM. Step 1: the pressure and temperature at the cavity inlet are defined. Step 2: the corresponding density is obtained by applying the ideal gas state equation. Step 3: the pressure and temperature inside the first cell are calculated by using the pressure and temperature equations. The equations are derived in detail in the later sections. Step 4: whether the cell has reached the tube outlet is determined. If yes, then the calculation is ended, and the results are outputted. Otherwise, we use the results of the previous cell as the initial conditions of the next cell and repeat steps 2-4.

The ideal state equation is

$$\rho = \frac{p\mathrm{M}}{\mathrm{RT}} \tag{4}$$

Here, M = 28.9634 g/mol is the molar mass of air, and R = 8.314 J/(mol·K) is the gas constant.

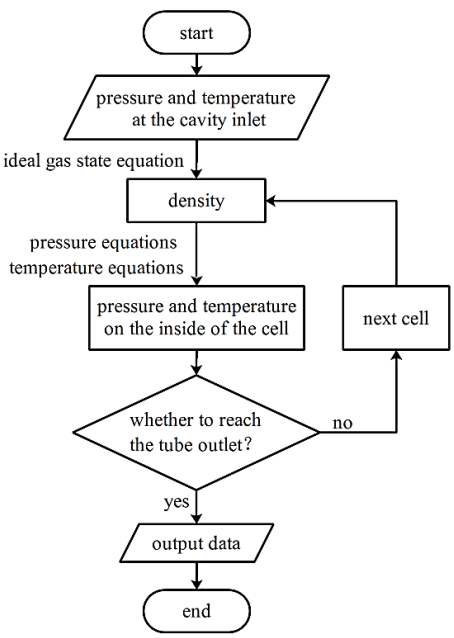

Fig. 12. Flow chart of the IACM.

4.2 Speed Prediction

Before analysing the velocity field, we established a theoretical flow structure based on the results of the numerical simulations, as shown in Fig. 13. After the airflow enters the co-rotating cavity, a pair of vortices with a boundary of r_s is formed near the shroud. Then, the airflow reaches the boundary, r_e, of the source region and flows to the two disks to form the Ekman boundary layers. Owing to the interference from the tube, the airflow converges at the tube inlet and flows radially inward to the tube outlet. The condition for the existence of boundary r_s is that the radial inward velocity of the airflow in the near-wall area is zero, and the condition for the existence of source boundary r_e is that the radial inward velocity of the airflow in the central region is zero.

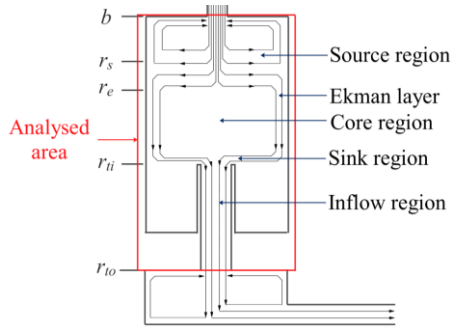

Fig. 13. Theoretical flow field structure in the tubed vortex reducer.

According to the conservation of angular momentum, the swirl ratio of the airflow in the source region satisfies the following equation:

$$Sr = cx^{-2} \tag{5}$$

Here, $x = r/b$. The inlet swirl ratio, c, is expressed as follows:

$$c = 1 - \frac{m\sin\theta}{n_s \rho \omega b \mathrm{A}_s} \tag{6}$$

Here, θ is the inclination angle of the shroud orifice, n_s is the number of the shroud orifices, and A_s is the flow cross-sectional area of the shroud orifice. In the tubed vortex reducer, c is 1.

Under engineering conditions, the airflow is in a turbulent flow state. Based on the linear Ekman boundary layer equations, Owen *et al.* (1985) obtained the swirl ratio in the core region under turbulent flow:

$$Sr = 1 + 2.22{\lambda_\mathrm{T}}^{5/8} x^{-13/8} \tag{7}$$

Here, λ_T is the turbulence parameter:

$$\lambda_\mathrm{T} = C_m / Re_\phi^{0.8} \tag{8}$$

By using Eqs. (5) and (7) simultaneously, we obtain the boundary of the source region as follows:

$${x_e}^2 = c - 2.22{\lambda_\mathrm{T}}^{5/8} {x_e}^{3/8} \tag{9}$$

Here, $x_e = r_e/b$.

In the tube, the flow is characterised by a rigid-body vortex; therefore, the swirl ratio in the tube is

$$\square\square=1 \tag{10}$$

4.3 Pressure Prediction

In the zone far from the boundary layer in the cavity, the radial and axial velocities of the airflow can be neglected. Hence, the pressure gradient along the radial direction exhibits the following relationship:

$$\frac{V_\phi^2}{r}=\frac{dp}{\rho dr} \tag{11}$$

The pressure drop in the cavity can be expressed as

$$\Delta p=\int_{r_1}^{r_2}\rho r\omega^2 Sr^2\,dr \tag{12}$$

Prior to this study, Firouzian *et al.* (1986), Farthing (1989 & 1991), and Chew *et al.* (1989) regarded the airflow in the flow field as an incompressible fluid. However, the assumption of incompressibility is valid only under high-pressure airflow and low-speed working conditions. To eliminate the influence of density, the pressure coefficient can be used:

$$C_p=\frac{2\Delta p}{\rho\omega^2 b^2} \tag{13}$$

Equation (13) is used to evaluate the pressure drop performance in the cavity; however, this does not provide more accurate information.

According to Fig. 9 and Fig. 10, the entropy increases rapidly owing to the sudden change in velocity at the tube inlet, indicating a large local loss. Figure 14 shows a schematic diagram of the velocity at the tube inlet. We approximated the radial velocity at the tube inlet as

$$V_{ri1}=\frac{m}{2\rho\pi r_{ti}S} \tag{14}$$

The radial velocity in the tube is

$$V_{ri2}=\frac{4m}{n_t\rho\pi d^2} \tag{15}$$

Equations (14) and (15) indicate that the radial velocity in the tube is considerably larger than that at the tube inlet.

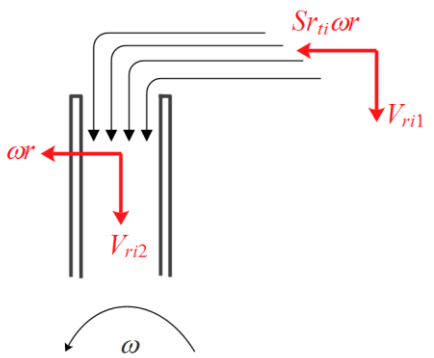

Fig. 14. Schematic diagram of the velocity at the tube inlet.

In the high-speed rotating cavity, the radial and axial velocities are significantly smaller than the tangential velocity. Thus, the local pressure loss at the tube inlet can be expressed as

$$\Delta p_{ti}=\frac{\rho[V_{ri2}^2+(\omega r_{ti})^2-(Sr_{ti}\omega r_{ti})^2]}{2}+\Delta p_{ir} \tag{16}$$

Here, Sr_{ti} is the swirl ratio at the tube inlet, and Δp_{ir} is the irreversible pressure drop. At the tube inlet, the airflow has a relatively high tangential velocity. However, the formula for calculating the irreversible pressure drop in the literature (Fried and Idelchik 1989) only considers the case of vertical intake. Consequently, we modified the irreversible pressure loss formula as follows:

$$\Delta p_{ir}=\frac{\xi_1\rho V_{ri2}^2+\xi_2\rho\left(Sr_{ti}{}^2-1\right)(\omega r_{ti})^2}{2} \tag{17}$$

Here, ξ_1 and ξ_2 are the loss coefficients:

$$\begin{aligned}\xi_1&=0.5\left(1-\frac{d^2}{8r_{ti}S}\right)\\ \xi_2&=1.1\left(1-\frac{d^2}{8r_{ti}S}\right)\end{aligned} \tag{18}$$

Equations (16)-(18) reveal that, when the relative tangential velocity of the airflow at the tube inlet is close to zero, the local pressure drop mainly originates from the pressure drop caused by the sudden increase in the radial velocity. As the relative tangential velocity at the tube inlet increases gradually, the irreversible pressure drop caused by the sudden change in the relative tangential velocity gradually increases. Equations (12)-(18) can be used to obtain the pressure coefficient, $C_{p.t}$, in the tubed vortex reducer as follows:

$$\begin{aligned}C_{p.t}&=2\int_{x_{ti}}^{1}Sr^2x\,dx\\&+\left(1.5-\frac{\mathrm{A}_t}{4\pi r_{ti}S}\right)\left(\frac{m}{n_t\rho\mathrm{A}_t\omega b}\right)^2\\&+\left(0.1-\frac{1.1\mathrm{A}_t}{2\pi r_{ti}S}\right)\left(Sr_{ti}{}^2-1\right)x_{ti}{}^2\end{aligned} \tag{19}$$

Here, A_t is the cross-sectional area of a single tube.

4.4 Temperature Prediction

In the rotating system, the energy equation of the stable open system can be written as

$$q=h_2-h_1+\frac{w_2^2-w_1^2}{2}+g(Z_2-Z_1)+\mathrm{w}_s \tag{20}$$

Here, q is the specific heat entering the control volume; h_1 and h_2 are the specific enthalpies at the inlet and outlet, respectively; w_1 and w_2 are the relative velocities; Z_1 and Z_2 are the heights; and w_s is the shaft power. Based on the assumption that the cavity walls are adiabatic and the weight force is neglected, Eq. (20) can be simplified to

$$0=h_2-h_1+\frac{w_2^2-w_1^2}{2}+\mathrm{w}_s \tag{21}$$

Because the Coriolis force and the relative velocity are perpendicular to each other, the Coriolis force does not contribute to the shaft work; thus, w_s can be expressed as

$$w_s = -\int_{r_1}^{r_2} \omega^2 r dr \tag{22}$$

Substituting Eq. (22) into Eq. (21) yields the following temperature change:

$$\Delta T = \frac{w_2^2 - w_1^2 + \omega^2 r_1^2 - \omega^2 r_2^2}{2Cp} \tag{23}$$

Here, Cp is the specific heat capacity at a constant pressure. We ignored the axial and radial velocities and incorporated the definition of the swirl ratio into Eq. (23). Thus, the temperature change can be expressed as

$$\Delta T = \frac{\omega^2[(Sr_2^2 - 2Sr_2)r_2^2 - (Sr_1^2 - 2Sr_1)r_1^2]}{2Cp} \tag{24}$$

Here, Sr_1 and Sr_2 are the swirl ratios at the inlet and outlet of the control volume, respectively. For the tubed vortex reducer, the temperature change, ΔT_t, in the cavity can be obtained as

$$\Delta T_t = \frac{\left(\frac{m}{n_t \rho A_t}\right)^2 + \omega^2(b^2 - r_{ti}{}^2)}{2Cp} \tag{25}$$

At the tube inlet, owing to the sudden change in velocity, the static temperature undergoes a sudden change. Section 3.3 describes that this abrupt phenomenon is present over a short radial distance. Thus, the work performed by the centrifugal force can be ignored. Thus, Eq. (21) can be written as

$$h_1 + \frac{1}{2}[(Sr_{ti} - 1)\omega r_{ti}]^2 = h_2 + \frac{1}{2}V_{ri2}^2 \tag{26}$$

The local temperature change at the tube inlet can be expressed as

$$\Delta T_{ti} = \frac{V_{ri2}^2 - [(Sr_{ti} - 1)\omega r_{ti}]^2}{2Cp} \tag{27}$$

4.5 Influence of the Parametrisation of the Calculation Cell

The IACM was used to establish the CPM for predicting the pressure, temperature, and density in the tubed vortex reducer. Theoretically, the size of *dr* directly affects the resolution and accuracy of the model. When the change in the density at the tube outlet with a decrease in *dr* is less than 0.2%, we consider that *dr* meets the requirements. Figure 15 shows the influence of the calculation cell size at design points 1 and 2. With a decrease in *dr*, the density at the tube outlet shows a slowly increasing trend. When *dr* is reduced from 1 mm to 0.5 mm, the density change is less than 0.2%. Because an aeroengine contains many components, a reasonable reduction in the calculation time for each component is beneficial for the entire model. Hence, we selected *dr* = 1 mm as a reference for the division of the calculation cell, considering both calculation accuracy and calculation time.

4.6 Calculation Procedure

Figure 16 shows the calculation process for the SPM. First, the structural parameters and boundary conditions should be obtained. Next, the swirl ratio in the cavity is calculated by using Eqs. (5), (7), and (10). Finally, the pressure distribution is calculated by using Eqs. (12) and (16). Figure 17 shows the calculation procedure for the CPM. Compared with the SPM, the CPM requires the temperature at the cavity inlet. Furthermore, the radius and width of the calculation cells in the cavity should be set in advance. Finally, the pressure, temperature, and density in the cavity are calculated by using the IACM.

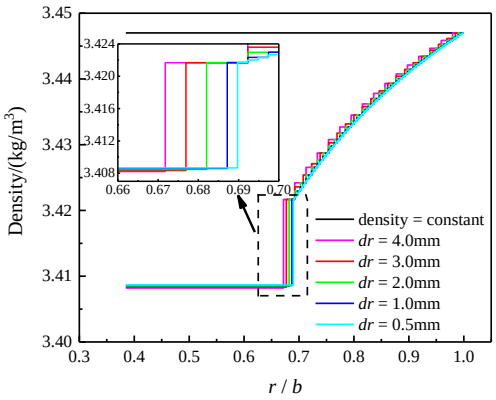

(a) Design point 1

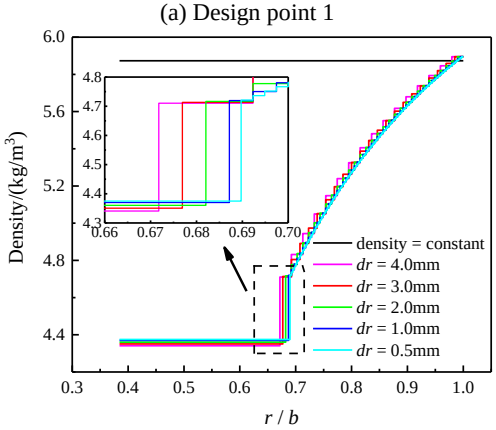

(b) Design point 2

Fig. 15. Influence of the computing cell size.

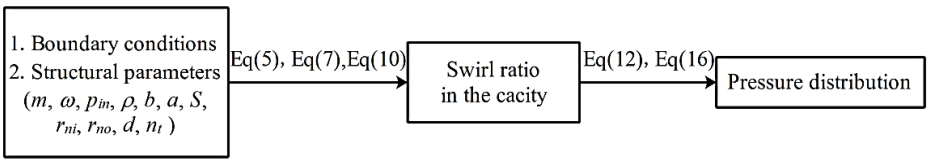

Fig. 16. Calculation procedure for the SPM.

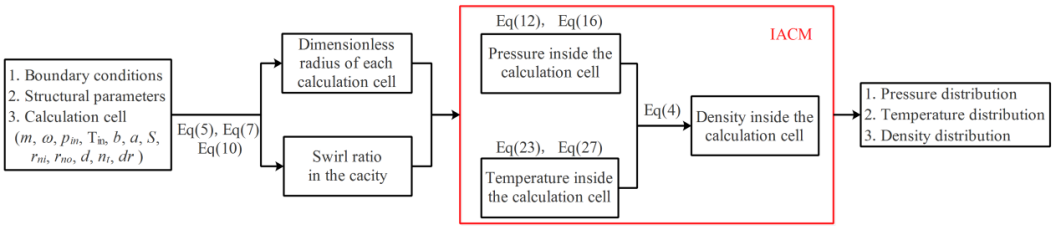

Fig. 17. Calculation procedure for the CPM.

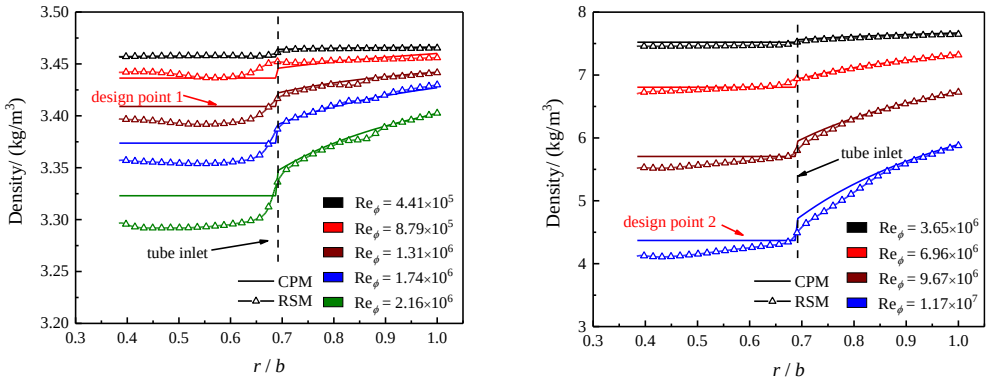

(a) Case 1 (b) Case 2

Fig. 18. Density distribution along the radial direction.

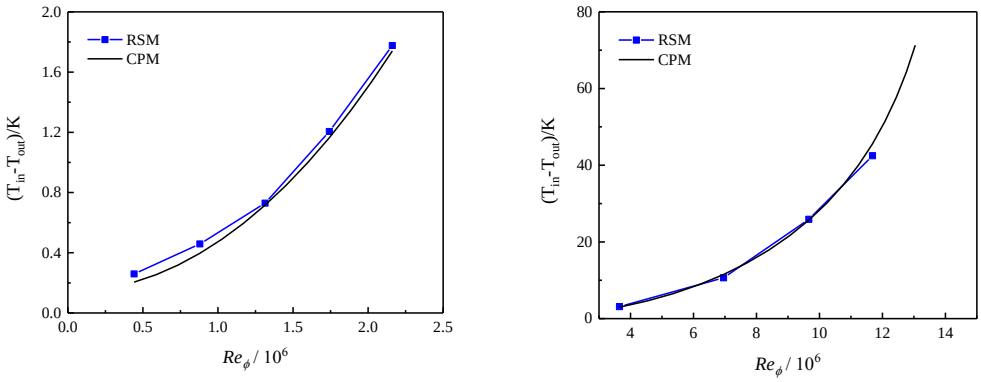

(a) Case 1 (b) Case 2

Fig. 19. Variation in the temperature change with the rotating Reynolds number.

5. RESULTS AND DISCUSSION

5.1 Aerodynamic Parameters

Figure 18 presents the density distribution in the tubed vortex reducer along the radial direction. The density decreases rapidly as the rotating speed is increased. At design point 1, the change in the density between the inlet and outlet is approximately 4.4%. At design point 2, this change is as high as 29.8%. To control the error expressed by Eq. (12), the airflow is considered to be incompressible only when the change in the density in the cavity is less than 8%. Thus, the airflow at design point 1 can be treated as an incompressible fluid, but it cannot be regarded as an incompressible fluid at design point 2.

In the cavity above the tube, the RSM results are consistent with those of the CPM. When the airflow enters the tube, the local loss causes a sudden drop in the density. Owing to the special treatment of the local loss of the CPM, the sudden change in the density in the CPM is more significant than that in the RSM. In the tube, the pressure and temperature reach a similar equilibrium state such that the density of the CPM results remains constant. In general, the IACM compensates for the shortcomings of the SPM.

In theory, the pressure and temperature are coupled parameters. Thus, an analysis of cavity temperature is necessary. Figure 19 illustrates the variation in the temperature change (T_{in}–T_{out}) in the tubed vortex reducer with the rotating Reynolds number. Owing

to the quadratic relationship between the centrifugal force and the rotating angular velocity, the temperature in the cavity decreases rapidly with an increase in the rotating Reynolds number. In case 1, the temperature change in the cavity is relatively low. Thus, the effect of temperature on the density can be neglected. In case 2, a strong centrifugal force causes a high temperature drop. According to Eq. (4), a decrease in temperature will increase the density; this value will be fed back to Eqs. (12) and (16) such that the pressure drop will increase. Overall, the relative mean error between the CPM and the RSM results is approximately 2.4%.

Figure 20 presents the temperature distribution in the tubed vortex reducer along the radial direction. In the cavity above the tube and in the region inside the tube, the temperature decreases rapidly. Owing to the stagnation effect of the airflow, the temperature suddenly increases at the tube inlet. Furthermore, the results of the CPM and RSM are generally similar, but there is a difference in the temperature at the tube inlet. Unlike at design point 1, Ekman boundary layers are present in the cavity above the tube at design point 2. Thus, the entropy at the bottom of the cavity increases rapidly such that the trough of the temperature curve in the RSM results is smoothed.

Figure 21 illustrates the variation in the pressure drop (p_{in}–p_{out}) in the tubed vortex reducer with respect to the rotating Reynolds number. According to Eqs. (12) and (16), the pressure drop in the cavity increases rapidly with the rotating Reynolds number. In case 1, the results of the CPM and SPM show good agreement with the RSM results. Owing to the small change in the density in the cavity, the SPM results are closer to the CPM results. However, in case 2, the SPM amplifies the error owing to the rapid decrease in the density, whereas the CPM still has a high prediction accuracy. Therefore, compared with the SPM, the CPM can be used in a wider range of working conditions.

Figure 22 presents the pressure distribution in the tubed vortex reducer along the radial direction. In the cavity above the tube, the pressure tends to decrease rapidly, and the decrease rate continues to increase. When the airflow enters the tube, the local loss causes a sudden drop in pressure. The results confirm that the local loss cannot be ignored. At design point 1, the local pressure drop accounts for a large portion owing to the weak centrifugal effect. However, at design point 2, the centrifugal and Coriolis forces are extremely strong such that the local pressure drop accounts for a small proportion. Furthermore, the error of the SPM at the tube inlet increases suddenly. As the radial height decreases further, the error of the SPM rapidly increases owing to the accumulation of

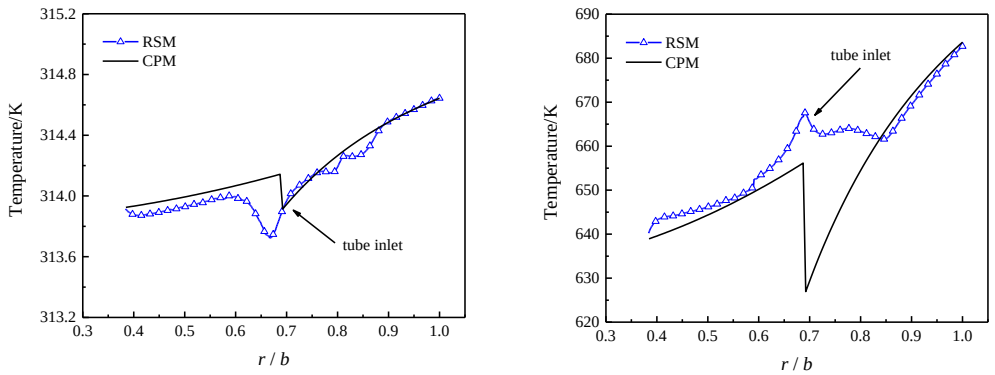

(a) Design point 1 (b) Design point 2

Fig. 20. Temperature distribution along the radial direction.

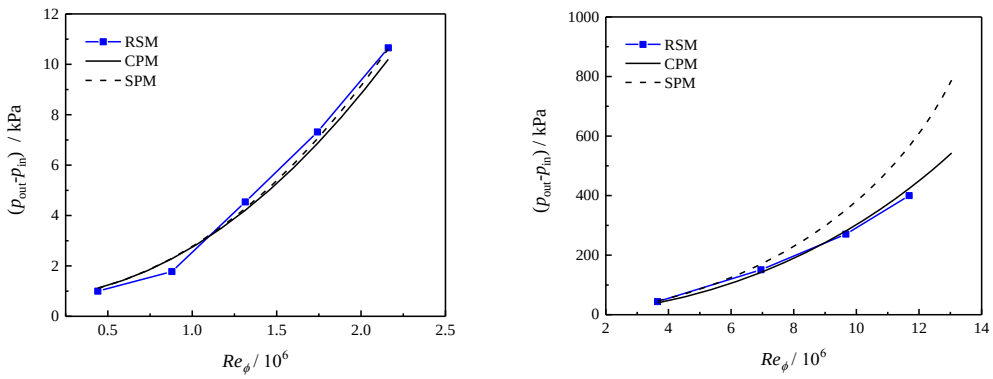

(a) Case 1 (b) Case 2

Fig. 21. Variation in the pressure drop with the rotating Reynolds number.

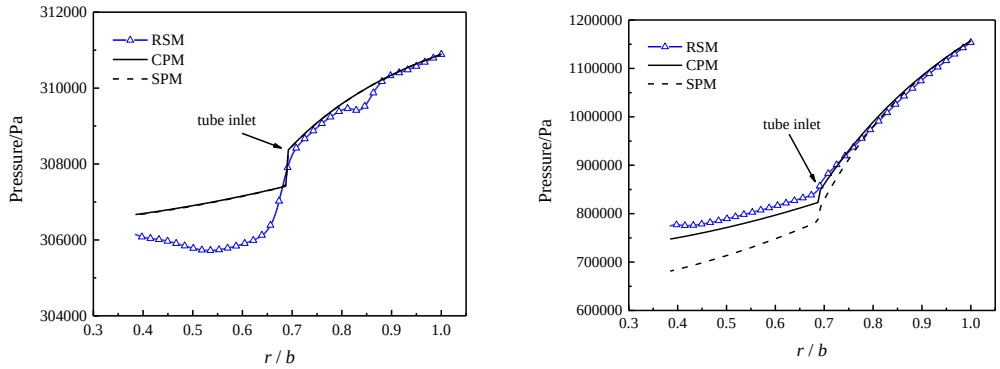

(a) Design point 1 (b) Design point 2

Fig. 22. Pressure distribution along the radial direction.

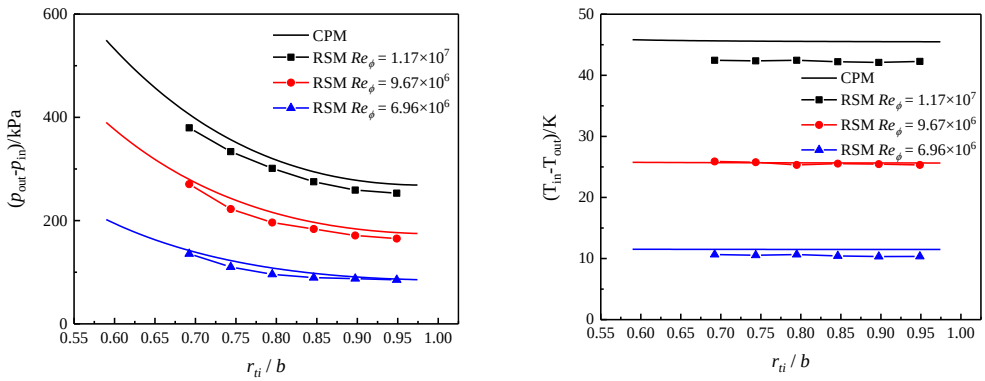

(a) Pressure drop (b) Temperature change

Fig. 23. Influence of tube length.

errors in the density. Compared with the SPM, the CPM can reduce the error by up to 71.57%.

The cruise performance is an indicator used to evaluate the performance of aeroengines. When the CFM 56-7B aeroengine is taken as an example, the rotating speed of the high-pressure compressor is approximately 15200 rpm under cruising conditions. For some small aeroengines, high-pressure compressors may have higher rotating speeds. Therefore, compared with the SPM, the CPM is more suitable for pre-design under all working conditions. Furthermore, the CPM requires less than 1 s to calculate the working condition, indicating that it has a high engineering value.

5.2 Structural Parameters

Figure 23 presents the effect of the tube length on the pressure drop (p_{in}–p_{out}) and temperature change (T_{in}–T_{out}). As the tube length is increased, the flow of the free vortex in the cavity is suppressed, and the local loss gradually decreases. Thus, the pressure drop decreases. When the tube inlet coincides with the cavity inlet, the local loss tends to be zero, and the pressure drop in the cavity reaches a minimum. According to Eq. (25), when the entire cavity is regarded as a control volume, the change in the tube length has no obvious effect on the temperature change. The weak effect is only reflected in the change in the radial velocity at the tube outlet.

Figure 24 illustrates the effect of the tube number on the pressure drop (p_{in}–p_{out}) and the temperature change (T_{in}–T_{out}). When the tube number is increased from 6 to 20, the local loss decreases, and the pressure drop in the cavity decreases by 9.8% on average. However, the weights of the tubes double. In addition, the effect of the tube number on the temperature change is negligible.

The vortex reducer should have not only good performance but also low weight. As depicted in the results in Fig. 24, reducing the tube number can substantially reduce the weight of the vortex reducer without causing a significant increase in the pressure drop. Theoretically, we can reduce the increased local loss caused by the reduction in the tube number by expanding the tube diameter. To compare the influence of the number and diameter of the tubes on the pressure drop and the temperature change, we propose the influence ratios, $\mathcal{L}_p$ and $\mathcal{L}_T$, which are defined as

$$\mathcal{L}_p = \frac{\partial C_p/\partial A_t}{\partial C_p/\partial n_t} \tag{28}$$

$$\mathcal{L}_T = \frac{\partial \Delta T/\partial A_t}{\partial \Delta T/\partial n_t} \tag{29}$$

The magnitude and sign of $\mathcal{L}_p$ can reflect the influence of the changes in A_t and n_t on C_p. When the absolute value of $\mathcal{L}_p$ is greater than 1, the influence

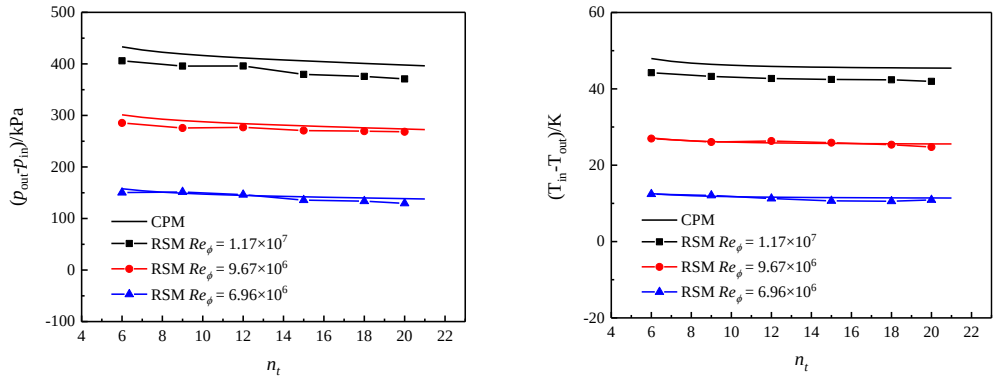

(a) Pressure drop (b) Temperature change

Fig. 24. Effect of the tube number.

of A_t on $\mathcal{L}_p$ is greater than that of n_t. Substituting Eq. (19) into Eq. (28) and Eq. (25) into Eq. (29) yields

$$\mathcal{L}_p = \frac{n_t}{A_t} + \frac{1}{4\pi r_{ti} S} \times \frac{1}{1.5 - \frac{A_t}{4\pi r_{ti} S}} \times \frac{n_t}{2} + \frac{1.1}{2\pi r_{ti} S} \times \frac{1}{1.5 - \frac{A_t}{4\pi r_{ti} S}} \times \frac{\left(Sr_{ti}{}^2 - 1\right) x_{ti}{}^2}{\left(\frac{m}{\rho A_t \omega b}\right)^2 \frac{1}{n_t{}^3}} \tag{30}$$

$$\mathcal{L}_T = \frac{n_t}{A_t} \tag{31}$$

In the tubed vortex reducer, n_t is considerably greater than 1 and A_t is significantly smaller than 1. Thus, the value of the first term in $\mathcal{L}_p$ should exceed 1. As the area of a single tube is smaller than the cross-sectional area of the cavity, the value of $\left(1.5 - \frac{A_t}{4\pi r_{ti} S}\right)$ should be greater than 0. Furthermore, Sr_{ti} is not less than 1, and the maximum tube length is the only case with $Sr_{ti} = 1$. Thus, the values of the second and third terms in $\mathcal{L}_p$ are greater than 0. Finally, we know that the value of $\mathcal{L}_p$ is greater than 1; therefore, the increase in the area of a single tube and the tube number is positive for the reduction in the pressure drop. The positive value of the area of a single tube is higher than the tube number. Similarly, we know that the influence of the area of a single tube on the temperature is higher than that of the tube diameter.

This analysis reveals that reducing the tube number and expanding the tube diameter simultaneously will not decrease the performance of the vortex reducer within a certain range. Meanwhile, the thickness of the tube wall is assumed to remain constant. In the aforementioned case, the total weight of the tubes may be reduced based on the geometric analysis. The matching of the tube diameter and tube number needs to be further studied.

5. CONCLUSION

In this study, a coupled model for predicting the pressure, temperature, and density in a co-rotating cavity with tubes was established. We verified its accuracy by employing the RSM and explored the influence of aerodynamic and structural parameters. The main conclusions are as follows.

1) The non-negligible local loss and entropy increase cause a sudden change in the pressure and temperature at the tube inlet, which is closely related to the rotating speed. Under low-speed working conditions, the sudden changes in the local pressure and local density are significant, and the local temperature decreases. As the rotating speed is increased, the sudden changes in the local pressure and local density weaken, and the local temperature increases.

2) The IACM, which predicts the density distribution in the cavity by using coupling pressure and temperature, compensates for the deficiency of the incompressibility assumption.

3) Compared with the single prediction model, the coupled prediction model that considers the compressibility of the airflow has higher prediction accuracy. With an increase in the rotating speed, the density in the cavity decreases, and thus, the error of the pressure prediction by the single prediction model rapidly increases. At design point 2, the coupled prediction model can reduce the error by up to 71.57%.

4) The increase in the length, number, and diameter of the tubes is beneficial for reducing the pressure drop but has no obvious effect on the temperature change. With an increase in the length, the pressure drop caused by the Coriolis force and the local loss shows a decreasing trend. With an increase in the number and diameter, the local loss gradually decreases.

The coupled prediction model established in this study is a multi-granularity mathematical model with the following three advantages: 1. the design of tubed vortex reducers is guided, and the development cycle is shortened; 2. the development of integrated aeroengine modelling is promoted; 3. reference data for research on the thermal stress and life of the disk are provided. The matching of the tube diameter and tube number needs to be further studied.

ACKNOWLEDGEMENTS

This research was supported by the National Science and Technology Major Project of China (grant No: 2017-III-0011-0037). And thanks to Y.X. Su and B. Ye for their contributions to the review.

REFERENCES

Chen, X., Y. Feng and L. Wu (2014). The experimental investigations of centripetal air bleed with tubed vortex reducer for secondary air system in gas turbine. *ASME Turbo Expo 2014: Turbine Technical Conference and Exposition*. Düsseldorf, Germany, GT2014-26959.

Chew, J. W. (1984). Prediction of flow in rotating disc systems using the k-ε turbulence model. *ASME Gas Turbine Conference*, Amsterdam.

Chew, J. W., P. R. Farthing, J. M. Owen and B. Stratford (1989). The use of fins to reduce the pressure drop in a rotating cavity with a radial inflow. *Journal of Turbomachinery* 111(3), 349-356.

Elena, L. and R. Schiestel (1996). Turbulence modeling of rotating confined flows. *International Journal of Heat and Fluid Flow* 17, 283-289.

Farthing, P. R., J. W. Chew and J. M. Owen (1989). The Use of De-Swirl Nozzles to Reduce the Pressure Drop in a Rotating Cavity with a Radial Inflow. *Journal of Turbomachinery* 113(1), 106-114.

Farthing, P. R. and J. M. Owen (1991). De-swirled Radial Inflow in a Rotating Cavity. *International Journal of Heat and Fluid Flow* 12(1):63-70.

Firouzian, M., J. M. Owen, J. R. Pincombe and R. H. Rogers (1985). Flow and heat transfer in a rotating cavity with a radial inflow of fluid, Part 1: The flow structure. *International Journal of Heat and Fluid Flow* 6(4), 228-23.

Firouzian, M., J. M. Owen, J. R. Pincombe and R. H. Rogers (1986). Flow and heat transfer in a rotating cylindrical cavity with a radial inflow of fluid, Part 2: Velocity, pressure and heat transfer measurements. *International Journal of Heat and Fluid Flow* 7(1), 21-27.

Fried, E and I. E. Idelchik (1989). *Flow resistance: a design guide for engineers*. New York, Hemisphere Publishing.

Gosman, A. D., F. C. Lockwood and J. N. Loughheadt (1976). Prediction of recirculating, swirling, turbulent flow in rotating disc systems. *Journal Mechanical Engineering Science* 18(3), 142-148.

Hide, R. (1968). On source-sink flows in rotating fluid. *Journal of Fluid Mechanics* 32(4), 737-764.

Jones, W. P. and A. Pascau (1989). Calculation of confined swirling flows with a second moment closure. *Journal of Fluids Engineering* 111, 248-255.

Kumar, B. G. V., J. W. Chew and N. J. Hills (2013). Rotating flow and heat transfer in cylindrical cavities with radial inflow. *Journal of Engineering for Gas Turbines & Power* 135(3), 2047-2060.

Liang, Z., X. Luo, Y. Feng and G. Q. Xu (2015). Experimental investigation of pressure losses in a co-rotating cavity with radial inflow employing tubed vortex reducers with varied nozzles. *Experimental Thermal and Fluid Science* 66, 304-315.

Morse, A. P. (1988). Numerical prediction of Turbulent of turbulent flow in rotating cavities. Journal of Turbomachinery 110, 202-211.

Onori, M., D. Amirante, N. J. Hills and J. W. Chew (2016). LES validation for a rotating cylindrical cavity with radial inflow. *ASME Turbo Expo: Turbomachinery Technical Conference and Exposition*, Seoul, South Korea. GT2016-56393.

Owen, J. M., J. R. Pincombe and R. H. Robers (1985). Source-sink flow inside a rotating cylindrical cavity. *Journal of Fluid Mechanics* 155, 233-265.

Poncet, S., R. Schiestel and M. P. Chauve (2005). Turbulence modelling and measurements in a rotor-stator system with throughflow. *Engineering Turbulence Modelling and Experiments* 185, 761-770.

Spalart, P. R. and M. Shur (1997). On the Sensitization of Turbulence Models to Rotation and Curvature. *Aerospace Science and Technology* 1(5), 297-302.

Torii, S. and W. J. Yang (1995). Numerical prediction of fully developed turbulent swirling flows in an axially rotating pipe by means of a modified k-ε turbulence model. *International journal of numerical methods for heat and fluid flow* 5(2), 175-183.

Wang, C., Z. Wang and J. Zhang (2020). Flow and heat transfer in a rotating cavity with de-swirl nozzles: An LES study. *International Communications in Heat and Mass Transfer* 118, 104816.

Wei, S., J. Mao, J. Yan, X. S. Han, Z. C. Tu and R. R. Tian (2020). Experimental study on a hybrid vortex reducer system in reducing the pressure drop in a rotating cavity with radial inflow. *Experimental Thermal and Fluid Science* 110, 109942.

Wei, S., J. Yan, J. Mao, X. S. Han and Z. C. Tu (2019). A mathematical model for predicting the pressure drop in a rotating cavity with a tubed vortex reducer. *Engineering Applications of Computational Fluid Mechanics* 13(1), 664-682.